PREPRINT: P. Moonen, B. Blocken, S. Roels and J. Carmeliet, Numerical modeling of the flow conditions in a closed-circuit low-speed wind tunnel, International Journal of Wind Engineering and Industrial Aerodynamics, Vol. 94, pp. 699-723, 2006. (doi:10.1016/j.jweia.2006.02.001). © Elsevier 2006.

Numerical modeling of the flow conditions in a closed-circuit low-speed wind tunnel

Peter Moonen * [(a)], Bert Blocken [(a)], Staf Roels [(a)], Jan Carmeliet [(a,b)]

(a) Laboratory of Building Physics, Department of Civil Engineering, Katholieke Universiteit Leuven, Kasteelpark Arenberg 40, 3001 Leuven, Belgium.
(b) Building Physics Group, Faculty of Building and Architecture, Technical University Eindhoven, P.O. box 513, 5600 MB Eindhoven, The Netherlands.

Abstract

A methodology for numerically simulating the flow conditions in closed-circuit wind tunnels is developed as a contribution to the general philosophy of incorporating Computational Fluid Dynamics (CFD) in wind tunnel design and testing and to CFD validation studies. The methodology is applied to the full-scale Jules Verne climatic wind tunnel in which experimental data have been obtained. Due to the specific features of this closed-circuit wind tunnel, the conventional CFD modeling approach, in which only the flow in the wind tunnel test section is modeled, is inadequate. To obtain accurate results the entire wind tunnel has to be modeled. In the numerical closed-circuit wind tunnel, the conventional flow inlet and outlet are replaced by a single "fan boundary condition". Special attention is given to the theoretical background and the practical implementation of this type of boundary condition in the CFD model. The numerical model is validated for the case of an empty wind tunnel and for the case in which a block-type building is placed in the test section. It will be shown that this methodology can generally reproduce the wind tunnel measurements of mean velocities with an error equal to or less than 10% despite the occurrence of multiple flow separations upstream of the test section. This provides perspectives for the future use of this methodology as a tool for wind tunnel design and testing and for CFD validation purposes.

Keywords: Computational Fluid Dynamics; CFD; Numerical simulation; Fan boundary condition; Wind tunnel design; Testing; Validation; Wind flow; Air; Building model; Test section flow quality

1 Introduction

Wind tunnel testing is a well-established discipline in Wind Engineering [1-6] and it is applied for a wide range of Wind Engineering studies [7-13]. In spite of the vast increase of computing performance in the past decades and contrary to what has been suggested in the past, CFD has not succeeded in replacing the wind tunnel, as adequately indicated by Meroney et al. [14] and by Stathopoulos [15]. In spite of not living up to earlier expectations, it can be stated that CFD has reached a stage in which its direct combination with the wind tunnel approach can yield a synergistic effect. On the one hand, wind tunnel measurements are being used to validate CFD calculations performed with different turbulence models, different near-wall modeling approaches, etc. On the other hand, CFD can be used as a tool to support wind tunnel design, wind tunnel testing and the interpretation of the test results. By far the most frequent exploitation of "wind tunnel–CFD synergy" in Wind Engineering has focused on wind tunnel testing for CFD validation. Numerous studies on this topic have been reported in the "Journal of Wind Engineering and Industrial Aerodynamics", in "Wind and Structures" and at the different Wind Engineering conferences. The use of CFD to support wind tunnel design and testing in Wind Engineering however has remained very limited up to now. An important contribution was made by Leitl and Meroney [16] who discussed the advantages of CFD simulations for the planning of dispersion tests in wind tunnels. The main use of CFD for wind tunnels has been situated in other research areas. Gordon and Imbabi [17] employed CFD to aid in the design of critical sections of a new wind/water tunnel for flow visualization purposes. Ghani et al. [18] used CFD to optimize and assess the performance of a number of key components of a climatic wind tunnel. In aeronautics, CFD has been used for the design of wind tunnel nozzles [19], for the interpretation of wind tunnel measurement results [20,21] and for better planning and utilization of wind tunnel tests [22].

In this paper, a numerical methodology is developed to model the flow conditions in closed-circuit wind tunnels, as a contribution to the general philosophy of incorporating CFD in wind tunnel design and

* Corresponding author: Peter Moonen, Laboratory of Building Physics, Department of Civil Engineering, Katholieke Universiteit Leuven, Kasteelpark Arenberg 40, 3001 Leuven, Belgium. Tel: + 32 (0) 16-321346 – Fax: + 32 (0) 16-321980. E-mail address: peter.moonen@bwk.kuleuven.be

testing and to CFD validation studies. In this approach, the entire wind tunnel configuration is incorporated in the CFD model. It differs from the traditional or "conventional" approach of modeling only the flow in the test section [23-25]. The methodology is applied and validated for the Jules Verne climatic wind tunnel in the framework of Wind Engineering research.

The paper starts with outlining the particular problem that raised the need for the development of a new methodology (Section 2). Section 3 describes the wind tunnel facility under study and the experimental results that were obtained. The numerical methodology is developed in section 4 and applied in section 5. In section 6, its importance is illustrated by comparing its results with results from a conventional CFD approach.

2 Problem statement

Wind tunnel testing for Wind Engineering purposes is typically performed in a boundary layer wind tunnel. Currently however, there is a general tendency to use specific wind tunnels as general-purpose wind tunnels for applications and studies that may be beyond their reach. An example is the use of "climatic" or "environmental" wind tunnels, primarily designed for testing for the automotive or building component industry, for wind engineering purposes (e.g. wind loading, wind-driven rain, pollutant dispersion, snow drifting). The problem is that the flow quality in these tunnels is generally less than that required for Wind Engineering studies. For a boundary layer wind tunnel, the following requirements can be set:

(a) The generation of a scaled and developed atmospheric boundary layer with adequate wind speed and turbulence profiles, which requires a sufficiently long fetch upstream of the test object;
(b) The absence of important flow separations in the wind tunnel circuit and especially in the sections directly upstream of the test section;
(c) Uniformity of the mean wind flow across the width of the test section and preferably also in the other parts of the wind tunnel;
(d) Low angularity, i.e. a mean flow direction that is approximately parallel to the test section center line;
(e) A sufficiently long length of the test section to allow for an accurate prediction of the upstream and downstream (wake) disturbance of the flow by the test object;
(f) Zero longitudinal pressure gradient;
(g) A blockage ratio smaller than 5% [26] and preferably smaller than 3% [23,27].

The latter three requirements concern both the test section dimensions and the dimensions and geometry of the test object. In other types of wind tunnels used for Wind Engineering studies, several of the above conditions will not be satisfied. In these situations there is an increased need for a thorough understanding of the impact of the wind tunnel design features on the flow in the test section and on the obtained results to guide their interpretation. CFD could then be used to obtain the information required. Generally, the numerical simulation of wind tunnel experiments is performed by modeling only the flow in the test section (rectangular computational domain) and by applying similar boundary conditions at the inlet as measured in the (empty) wind tunnel test section. However, if the above conditions are not satisfied, this "conventional" approach may no longer be adequate and a more extensive CFD modeling methodology is required.

As an example the study in this paper focuses on the "Thermal Circuit" of the full-scale Jules Verne climatic wind tunnel facility of the CSTB (Centre Scientifique et Technique du Bâtiment) in Nantes, France. This exceptional wind tunnel is particularly well suited for full-scale testing of the performance of vehicles and building components under different climatic conditions. As part of the European Commission 4th Framework Programme (Training and Mobility of Researchers, Access to Large-Scale Facilities – Access for researchers, 1994-1998), this facility was made available for a number of Wind Engineering studies. The fact that a number of the above-mentioned requirements were not satisfied raised the need for a thorough understanding of the wind tunnel flow characteristics and of their influence on the obtained experimental results. Given the specific configuration of the Jules Verne Thermal Circuit, this information can not be obtained with the "conventional" modeling approach. Instead, modeling the entire wind tunnel is required to obtain useful information.

3 Wind tunnel facility, test set-up and results

3.1 Wind tunnel facility

The Jules Verne climatic wind tunnel facility consists of two separate concentric wind tunnels. The outer tunnel or "dynamic circuit" (operational since October 1990) and the inner tunnel or "thermal circuit" (operational since March 1995). Both tunnels allow conducting extensive full-scale experiments.

In the thermal circuit, a wide range of real-life climatic conditions like rain, snow, frost and solar radiation can be simulated [28]. All experimental data used in this paper were acquired in the thermal circuit.

The configuration of the thermal wind tunnel is shown in Fig. 1. Fig. 1a is the plan view. Fig. 1b and d are a longitudinal and a lateral cross-sectional view. Fig. 1c is a photograph of the nozzle, screen and guiding vanes. The different sections of the wind tunnel are briefly described, starting from the test section and moving in the downstream direction. Numbers are used to refer to the different features. The test object (1) is positioned in the test section (2). This section has a rectangular cross-sectional area of W x H = 10 x 7 m² and a length of 25 m. A sudden contraction (3) connects the downstream end of the test section to a 180° turn (4). The turn has a 6 x 7 m² rectangular cross-section at the outlet of the test section, which gradually widens to 7 x 7 m² at the fan-straightener section. A highly porous safety net (5) is situated at the end of the turn to prevent model parts entering the fan-straightener section and damaging the fan in case of model failure. Upstream of the fan there is an abrupt transition (6) from the rectangular to a circular cross-section (diameter 6.2 m) to take the flow into the fan. The fan itself (7) is a large axial variable-revolution fan (1000 kW) that can create stationary wind flow within a range of 1 to 38 m/s. Flow straighteners (8) are present downstream of the fan blades to remove the swirl generated by the fan. Behind the fan-straightener section, there is a smooth transition of the cross-section from circular back to rectangular (7 x 9 m²) by means of a small-angle diffuser (9). At the end of the diffuser, a heat exchanger is installed (10). The second 180° turn gradually reduces the cross-sectional area to 6 x 9 m². At the end of the turn (11), two horizontal and six vertical guiding vanes (12) are present to force the incident wind flow to be approximately parallel to the test section center line and to increase the flow uniformity across the test section width. Immediately downstream of the vanes, a screen (13) is installed (see Fig. 1c, d). It is composed of wooden slats with dimensions 40 x 20 mm that span the entire nozzle width. The spacing between the slats increases from bottom (50 mm) to top (350 mm). Note that this screen is not a permanent feature of the wind tunnel. It was only installed for the Wind Engineering tests to generate vertical wind speed and turbulence intensity gradients that show a certain degree of similarity with those found in an atmospheric boundary layer. The adjustable nozzle (14) provides a contraction from the cross-section at the end of the second turn (6 x 9 m²) to a cross-sectional area that can range from 6 x 5 m² to 6 x 3 m². This contraction is realized by suddenly lowering the height of the ceiling over a distance between 3 to 5 m and by raising the floor level by 1 m. Downstream of the contraction, a (very) short set of roughness elements is positioned (L x W = 4 x 6 m²), consisting of densely spaced cubes of 50 mm height (15). At the exit of the nozzle, the wind flow discharges into the larger test section (2).

The configuration of this climatic wind tunnel deviates in a number of aspects from that of a boundary layer wind tunnel and does not comply with several of the requirements mentioned in section 2: (a) The generation of an atmospheric boundary layer is complicated by the very short fetch and by the disturbances (e.g. flow separation) in the flow upstream of the test section; (b) Flow separation will occur in several sections, e.g. due to sudden changes in cross-sectional area, such as in the nozzle section, at the entrance of the test section, at the exit of the test section and at the transition in cross-sectional area upstream of the fan. In addition, flow separation will also occur in the 180° turns; (c-d) The flow disturbances caused by the flow separations compromise the achievement of a laterally uniform flow (honeycombs are not present) with low angularity; (e) At least for bluff bodies, an optimal choice of the up- and downstream distances to respectively the in- and outlet of the test section is compromised by the relatively short test-section length, as compared to its cross-sectional dimensions. The limited downstream length can compromise an accurate reproduction of the wake; (f) A longitudinal pressure gradient will exist causing horizontal buoyancy on the test object [26]. These aspects have a pronounced influence on the flow in the test section and on the obtained results, as will be shown in the remainder of this paper.

3.2 Test set-up

Two sets of experiments were conducted: measurements in the wind tunnel with empty test section (free-runs) and measurements around a block-type building model placed in the test section.

In the free-run experiments, wind speed measurements were performed along four vertical lines located at positions P01 to P04 near the entrance of the test section, at intervals of 0.3 m up to 4.8 m height (Fig. 2a and Table 1). The measurements were performed by means of an unidirectional hot-wire anemometer, yielding mean wind speed and longitudinal turbulence intensity (I_U) at 4 x 16 measurement points, and were repeated for three different flow regimes, with wind tunnel setting speed 1.6 m/s, 3.6 m/s and 5.5 m/s.

The second set of experiments included wind velocity measurements around a block-type building (w x d x h = 3 x 2 x 2 m³) positioned at 6 m from the nozzle exit as a compromise between upstream and downstream distance from the building in the test section. The blockage ratio is 8.6 %. As a result, the flow field around the test building will be significantly influenced by the presence of the wind tunnel walls. At 6 positions around the test building ultrasonic anemometers were installed (see Fig. 2b and Table 1). Measurements were performed at the same three flow regimes as for the free-runs. The three components of the instantaneous velocity vector (u, v, w) were monitored yielding values of mean velocity (U, V, W) and turbulence intensity (I_U, I_V, I_W) in the three main directions (Eq. 1 and 2):

$$U = \frac{1}{n}\sum u \tag{1}$$

$$I_U = \frac{\sqrt{\frac{1}{n}\sum (u-U)^2}}{\sqrt{U^2+V^2+W^2}} \tag{2}$$

Where n is the number of measurement data. The other components are obtained in the same way.

3.3 Test results

3.3.1 Empty wind tunnel

The results in Fig. 3 illustrate the vertical wind speed profiles (Fig. 3a) and the vertical turbulence intensity profiles (Fig. 3b) at position P01 for the three flow regimes. Especially the turbulence intensity profile deviates from a typical profile – it should show a significant decrease with height. This deviation results from the specific geometrical features of the wind tunnel which – among others – yield flow separation at the nozzle exit. At this position, the shear effect at the junction between the jet stream and the stagnant air above yields an increase in turbulence intensity at approximately 5 m height above the test section floor. The turbulence intensity peak at 3.9 m height is caused by the upper horizontal guiding vane, which is positioned at approximately the same height (Fig. 1b, c). The effect of the lower guiding vane is suppressed by the presence of the wooden screen downstream of it.

In an ideal situation the flow in the test section is laterally uniform and parallel to the test section center line. Fig. 4 seems to indicate that the wind speed profile is approximately uniform over the width of the nozzle (the wind speed at P03 is only slightly higher) whereas the turbulence intensity profile is clearly not. Later in this paper however, it will be shown that the wind speed profile is not uniform over the width of the nozzle either. The reason for the particular observations in Fig. 4 is the position of point P03 relative to the outer vertical guiding vane. In fact, the vanes are added to increase the flow uniformity, but it appears that their presence itself introduces a significant amount of turbulence, which was also shown earlier for the upper horizontal guiding vane. The same occurs for the outer vertical guiding vane. This is the direct cause for the anomalous turbulence profile P03 in Fig. 4b.

3.3.2 Wind tunnel with building model

Table 2 contains the measured values of the mean velocity components (U, V, W) and the turbulence intensity values (I_U, I_V, I_W) at points A-F around the block-type building model. The wind speed values are made dimensionless with respect to the streamwise reference wind speed U at point A and are averaged over the three flow regimes (1.6 m/s, 3.6 m/s and 5.5 m/s). The turbulence intensities, averaged over the flow regimes, are given as well. Comparing the velocity components at points A and B, a decrease of the streamwise wind velocity component U and an increase of the vertical component V are observed. The lateral component W at these points is small, indicating that the incident wind flow is approximately parallel to the test section center line. Points C and D are positioned symmetrically with respect to the center line. Consequently the absolute values of the measured quantities are similar. The turbulent fluctuations are larger at point D than at point C. This observation is consistent with the free-run experiments and confirms the assumption that the outer vertical guiding vane introduces a significant amount of turbulence. Point E is situated in the corner stream/separation region. Higher mean velocities and increased turbulence intensities are found here. Point F is the only measurement point at 1.18 m height. Lower mean wind speed and higher turbulence intensities are observed at this position.

4 Numerical methodology

Given the configuration of the wind tunnel and the observed flow conditions, the conventional approach of modeling only the flow in the test section is inadequate, as will be shown later in this paper. It is replaced by the approach of modeling the entire wind tunnel to take into account the influence of the

specific features of the flow in the entire circuit (e.g. flow separation) on the results obtained in the test section (Fig. 5). In this approach, the conventional flow inlet and outlet are replaced by a single "fan boundary condition". It will be shown that the parameters for this type of boundary condition can be easily determined, based on only one preliminary calculation, which is an important aspect in favor of the developed methodology.

4.1 Theoretical background

In each section ℓ of the wind tunnel circuit, a certain amount of mechanical energy is converted to heat. These local losses cause a drop in total head. The total pressure loss in the wind tunnel is given by Eq. (3):

$$\Delta P_{tot} = \sum_{\ell} R_{\ell}(v)\, L_{\ell} \tag{3}$$

where v (m/s) represents the area-weighted average value of the streamwise wind speed (averaged over the cross-sectional area of the local section ℓ as defined by Barlow et al. for a one-dimensional analysis of wind tunnel energy performance [26]), R_{ℓ} (Pa/m) is the local loss per unit length in section ℓ and L_{ℓ} (m) is the section length. R_{ℓ} is a function of wind speed. The function $R_{\ell}(v)$ is mainly determined by the geometry of the wind tunnel. It can be shown that the losses in pressure are proportional to the kinetic energy per unit volume of air ($\rho v^2/2$). Consequently, for a given geometry of the wind tunnel, the pressure needed to maintain a certain flow rate is proportional to the square of the flow rate G_a (m^3/s):

$$\Delta P_{tot} = \xi G_a^2 \tag{4}$$

where ξ is a loss coefficient, mainly determined by the geometry of the wind tunnel. Eq. (4) is called the wind tunnel system curve. It describes the relationship between the flow rate in the system and the corresponding pressure loss (Fig. 6). Every point on this curve corresponds to a possible operating point of the wind tunnel. The actual operating point is the result of the interaction between the wind tunnel geometry and the fan. The full complexity of the problem is described by the coefficient ξ. The analytical derivation of the expression for ξ is only possible for relatively simple situations.

In order to create a stationary wind flow through the tunnel, the pressure losses must be overcome by the pressure rise by the fan. The relation between the pressure rise generated by the fan and the flow rate through it is described by the fan performance curve (Eq. 5).

$$\Delta P_{fan} = f(G_a) \tag{5}$$

The actual shape of the function f is dependent on the type and design of the fan. It is typically a decreasing function of the flow rate G_a for a certain fan speed, as indicated in Fig. 6. Indeed, at increasing levels of counter pressure, the corresponding flow rate a fan can deliver decreases. In the wind tunnel a stationary flow regime is obtained when the total pressure loss in the tunnel (given by Eq. 4) is balanced by the pressure rise over the fan (given by Eq. 5):

$$\xi G_a^2 = f(G_a) \tag{6}$$

The operating point can thus be found as the intersection between the system curve and the fan performance curve. In fact, there is not a single operating point, but an entire operating region, because increasing the fan speed increases both flow rate and pressure. This causes the fan performance curve to move upwards until a new equilibrium is reached, as indicated by the different fan performance curves in Fig. 6.

4.2 Implementation of the system curve

The geometry of the numerical wind tunnel is based on the full-scale geometry of the actual wind tunnel. In this way, the system curve is implicitly implemented in the model. The better the correspondence between the real geometry and the numerical model, the better the behavior of the latter will agree with that of the existing tunnel. An exact implementation would require modeling all geometrical details, which is not possible from a practical and economical point of view. The following simplifications were adopted:

(a) The walls, floor and roof of the wind tunnel are modeled as solid walls with a certain roughness height and roughness constant (Table 3). For the set of roughness elements at the end of the nozzle floor, the physical roughness height K_S is set to 0.05 m. For the other walls a roughness $K_S = 10^{-3}$ m is adopted, except for the guiding vanes ($K_S = 10^{-6}$ m). The roughness constant C_{KS} is taken 0.5 in all cases.

(b) The fan-straightener section, including fan nacelle, fan blades and flow straighteners is not modeled in detail. It is replaced by a so called "fan boundary condition", which will be explained in section 4.3. No swirl modeling is included because of the presence of the fan flow straighteners.
(c) The relation between pressure drop over and flow rate through the heat exchanger is not known. It is also not clear whether it will increase or reduce turbulence. In first instance, it is chosen not to model the heat exchanger and to assess the influence of replacing the combination of fan-straightener section and heat exchanger by the single fan boundary condition mentioned above by validation with the measurements.
(d) Because the "fan boundary condition" can be imposed on a cross-sectional surface of arbitrary shape, it was chosen to not model the abrupt transition from rectangular (7 x 7 m²) to circular (Φ = 6.2 m) in the fan-straightener section, nor the smooth transition back to a rectangular cross-section (7 x 9 m²) in the small angle diffuser. Instead the fan-straightener section is modeled with a rectangular shape (7 x 7 m²) over its entire length (4 m). The small-angle diffuser is modeled with a rectangular cross section that gradually widens from 7 x 7 m² to 7 x 9 m² (Fig. 1a).
(e) The highly porous safety net upstream of the fan is not included in the model.

All other details, including the horizontal and vertical guiding vanes and the wooden screen at the entrance of the test section are modeled in detail. The validity of the above-mentioned simplifications was ascertained by sensitivity analyses. These comprised a systematic comparison of the results from the simplified model with results from more detailed models in which, respectively, different roughness heights were applied, the fan nacelle was included, and the transition of the cross-sectional area in the fan section from rectangular to circular and back to rectangular was implemented. The analyses showed that the influence of the roughness height is very limited and that the influence of omitting the fan nacelle and the transition rectangular-circular-rectangular in the model is significant for the flow in the fan section itself – as expected – but not for the flow in the test section. On the other hand, accurately modeling the guiding vanes and the wooden screen had a large impact on the flow pattern in the test section. Consequently these features have to be taken into account in the numerical model. The simplified geometry is shown in Fig. 5a.

4.3 Implementation of the fan performance curve

The fan performance curve is implemented by means of a polynomial of arbitrary order. It relates the pressure rise over the fan, the fan area and the flow rate. For simplicity, a linear function is chosen here, but any function could be used:

$$\Delta P_{fan} = f\left(G_a\right) = a_0 + a_1 \frac{G_a}{A_{fan}} \tag{7}$$

Eq. (7) does not represent a realistic fan performance curve (as those given in Fig. 6). However, the adopted shape of the fan performance curve does not affect the obtained results, as long as it intersects the system curve at the required operating point. Fig. 7 illustrates three different fan performance curves that give exactly the same flow conditions in the numerical wind tunnel. The shape of the fan performance curve does influence the transient wind-flow pattern towards the operating point, but not the stationary wind-flow pattern at that point. It was observed that the shape of the fan performance curve has a pronounced influence on the convergence rate of the CFD calculation. E.g. selecting the (unrealistic) fan curve with the positive slope in Fig. 7 yields a calculation that takes 2.5 times longer than the other two fan curves, which yield about the same convergence rate. In the remainder of this paper, a horizontal fan curve will be used.

4.4 Two-step calculation methodology

Two CFD calculations are needed to obtain the flow conditions in the wind tunnel at the same operating point at which the measurements were conducted. The objective of the first one is to determine the loss coefficient ξ. For this calculation, "arbitrary" values for the coefficients a_0 and a_1 in Eq. (7) are selected. The flow quantities are given an initial value (in this case: set to 0) and the problem is solved using CFD. When convergence is obtained, the pressure jump ΔP_{tot}' over the fan is equilibrated by the head losses in the wind tunnel corresponding to a certain flow rate G_a'. As a result the wind tunnel is working at the operating point (ΔP_{tot}', G_a'). This point will generally be different from the one at which the experiments were done, but it allows to determine the friction coefficient ξ using Eq. (4) and hence the shape of the system curve. From this curve and the knowledge of the flow rate at which the experiments were conducted, the actual pressure rise ΔP_{tot} that is required by the fan is obtained (Eq. 4).

Two new coefficients a_0 and a_1 for the fan performance curve are selected in such a way that this curve intersects the system curve at the actual operating point (ΔP_{tot}, G_a). The CFD solution with this new fan curve yields the required result.

Note that two calculations would not be necessary if the flow pattern in the circuit and the loss coefficient were independent of the Reynolds number. In this case, the velocity field could be linearly scaled with respect to a reference wind speed in the tunnel. For the given configuration however, with rounded shapes and multiple flow separation, Reynolds number dependency can occur within a certain range of flow rates. For this reason, it is also preferred that the chosen fan performance curve for the preliminary calculation intersects the system curve at a point that is situated not too far from the actual operating point of the wind tunnel.

4.5 Computational mesh

An attempt was made to combine the advantages of a structured grid (less numerical diffusion when aligned with the flow, better accuracy near wall boundaries) with those of an unstructured grid (meshing complex geometrical features, clustering of cells in regions where needed). Those sections of the wind tunnel that are of simple geometry and in which one-dimensional flow dominates were meshed with structured prismatic elements. In the sections of complex geometry and where pronounced three-dimensional flow patterns develop, like in the neighborhood of the guiding vanes and roughness screen, tetrahedral elements are used. To capture the steep velocity gradient near the wind tunnel walls, the tunnel was meshed using a tube-in-tube meshing system. The outer tube has a thickness of 0.15 m. The grid resolution is determined taking into account an acceptable value for the dimensionless wall unit y^+ (average value of 250), the physical roughness height K_S (ranging from 10^{-6} to 10^{-2} m), the equiangle and equivolume skewness of the cells (average value of 0.3) and the occurring velocity gradients. The grid in the inner tube is generally coarser and adapted to the core flow: the larger the expected velocity gradients, the smaller the grid size. The maximal expansion ratio between the sizes of neighboring cells is 1.3. A grid sensitivity analysis was performed to obtain a suitable numerical grid, both for the case of the empty wind tunnel and for the case of the wind tunnel with the building model in the test section. Table 4 summarizes the number of control volumes for the tested grids. Part of the grid is displayed in Fig. 8a and b. Accurately modeling the guiding vanes and the screen (slats with 0.04 m thickness) required a very high mesh resolution at these locations. Table 5 indicates the distribution of the number of control volumes over the different sections in the wind tunnel.

4.6 Solution method

The three-dimensional Reynolds-Averaged Navier-Stokes (RANS) equations and the continuity equation were solved using the commercial CFD code FLUENT 5.4 that employs the control-volume technique. Closure is obtained by using a k-ε turbulence model. Near-wall modeling was performed using wall functions. For the present study, the use of the standard [29] and the realizable k-ε turbulence model [30] showed no significantly different results, as was also the case for standard wall functions [31] versus non-equilibrium wall functions [32]. Pressure-velocity coupling was taken care of by the SIMPLEC algorithm [33]. Second order pressure interpolation was used. The QUICK discretization scheme was used for the convection terms of the governing equations and the equations of the turbulence model [34]. The calculations were performed on a 3GHz Pentium 4 workstation and required 440 Mb of RAM. Typically 2000 iterations (10 hours CPU) were needed to reach the desired level of convergence (residuals down to 10^{-4} or less) with a horizontal fan performance curve. The residuals are defined as the imbalance of the conservation equations summed over all control volumes or cells. These values are scaled and the scaled values are used in the code as a measure of the iteration convergence [35].

5 Application and validation

5.1 Empty wind tunnel

The CFD calculation to determine the loss coefficient ξ was conducted with a fan performance curve with coefficients a_0 = 10 Pa and a_1 = 0 Pa.s/m. Based on the obtained value for ξ (= 6.53 10^{-4} Pa.s^2/m^6), three other calculations were conducted with coefficients a_0 = 1.78, 7.49 and 18.00 Pa and a_1 = 0 Pa.s/m, resulting in flow rates of respectively 52.2, 107.1 and 166.2 m³/s. These operating points are close to the actual operating points in the experiments at the three velocity regimes. No Reynolds number dependency could be observed within this range of flow rates. The results are described below.

Fig. 9a and b show contours of dimensionless wind speed (magnitude of 3D velocity vector) in a horizontal plane at a height of 1.75 m and in a vertical plane along the test section center line respectively. The values are made dimensionless with respect to the streamwise wind speed U at 2.1 m height on the

vertical line P01 (Fig. 2a). It is clear that the flow field is not uniform over the width of the test section and that the wind speed changes considerably along the length of the section. Furthermore Fig. 9c shows that the outer vertical guiding vane causes a significant increase in local wind speed due to flow separation at its leading edge and that its wake extends for a considerable distance downstream. This explains two phenomena: (a) The apparent contradiction between the wind speed measurements in Fig. 4a that do not show a pronounced lateral non-uniformity at the positions P01, P02 and P03 and Fig. 9a that does show a pronounced lateral non-uniformity. The reason is that the lines P01 and P02 are situated outside the region with the largest wind speed and that the line P03 is situated in the wake of the outer guiding vane, where a local decrease in wind speed is present; (b) The increased turbulence intensity that was found at point P03 (Fig. 4b).

Fig. 10 compares the numerical results (wind speed) with the corresponding measurements. The relative error between both datasets is generally less then 10%. This is small compared to what one may expect from a k-ε model, especially taking into account the multiple flow separation in the wind tunnel and at the nozzle entrance and exit in particular.

Fig. 11 compares the turbulence intensity data at P03 and P04. The profiles for P03 are specifically shown here because this profile is situated in the wake of the outer guiding vane. It shows the worst correspondence between measurements and calculations (Fig. 11a). The most likely reason is a discrepancy in modeling the geometry (shape and direction) of this guiding vane. The measurements indicate that this vane is misaligned, giving rise to a wake behind it with increased turbulence intensity (Fig. 4b). In the calculations, the misalignment was not included. Note that at the three other locations, a fairly good agreement is obtained, although the turbulence level is somewhat underestimated (e.g. Fig. 11b). This might be due to the effect of the heat exchanger which was not included in the model.

5.2 Wind tunnel with building model

The same procedure is employed as mentioned above. The first calculation with a fan performance curve with coefficients a_0 = 10 Pa and a_1 = 0 Pa.s/m yields $\xi = 7.62\ 10^{-4}$ (Pa s^2)/m^6. The obtained loss coefficient is 16.8 % higher than the value found in the case of the empty wind tunnel which is due to the increased flow resistance by the presence of the building. The simulations around the building model were carried out with the following coefficients: a_0 = 2.08, 8.74 and 21.10 Pa and a_1 = 0 Pa.s/m yielding the same flow regimes as in the case of the empty wind tunnel (flow rates of 52.2, 107.1 and 166.2 m^3/s). No Reynolds number dependency could be observed.

Fig. 12a and b illustrate the contours of dimensionless wind speed (magnitude of 3D velocity vector) in a horizontal plane at 1.75 m height and in a vertical plane along the test section center line. The wind speed is made dimensionless with respect to the streamwise velocity component U at point A (Fig. 2b). The high blockage ratio results in corner streams with high wind speed values and the wake is forced to close at the outlet of the test section. Due to the lateral non-uniformity of the incident flow field, the wind speed values in the corner streams have different magnitudes. Fig. 13 compares the numerical results with the measurements. A good agreement is obtained. The error is less than 10% for all velocity components, except two: the x-velocity component at point B and the z-velocity component at point E. The deviation at point B is probably due to a small misalignment of the ultrasonic anemometer as was noticed during the measurements. The error on the lateral velocity component in point E can be attributed to the combination of overproduction of the turbulent kinetic energy by the k-ε model and a possible measurement error. The measured turbulence intensity is generally reproduced with a relative error of less than 20% except for point F, where the turbulence is underestimated by approximately 40% (Fig. 14). The overall performance of the numerical model however is good.

In the next section, the difference in results between the proposed methodology and the conventional CFD approach of modeling only the flow in the test section is shown.

6 Comparison: open rectangular versus closed-circuit computational domain

6.1 Conventional approach

In the conventional approach an open rectangular computational domain is employed, the width and height of which are usually taken equal to the tunnel dimensions to match the blockage ratio of the experiments [23]. The sizes of the upstream disturbance and the fully developed wake determine the length of the computational domain. As a result, for the case of the Jules Verne wind tunnel, a conventional computational domain with dimensions W x D x H = 10 x 33.2 x 7 m was constructed (Fig. 5b). The building was positioned at 6 m from the inlet, as in the experiments. The downstream length allowed the wake to close. The conventional approach requires specifying boundary conditions at both the inlet and the outlet of the domain. A set of wind tunnel measurements usually only comprises the

measurements of the approach flow profile at one location in the test section. Likewise, in this simulation, it was assumed that only the P01 profiles were available. These profiles were used at the inlet. At the outlet zero static pressure was set. The roughness of the walls, floor and top of the computational domain was set according to Table 3. The resolution and structure of the computational mesh were taken equal to those used in the test section of the closed-circuit domain, yielding 178 563 cells for the empty wind tunnel and 185 976 cells for the wind tunnel with building model. The solution is obtained with the same settings as mentioned in section 4.6 (turbulence model, wall functions, pressure-velocity coupling, discretization schemes).

6.2 Comparison

Fig. 15 compares the measured x-velocity components (U) for all 6 measurement points around the building model with the corresponding calculations in a rectangular (r) and in a closed-circuit (c) domain. The dotted lines indicate the deviations of the numerical results from the measurements, relative to the measured values. Note that the calculations in the closed-circuit domain are all within 10% of the measured quantities, except for point B. As expected, the conventional approach yields significant deviations that are 2 to 4 times higher. Similar observations hold for the y- and z-velocity components.

The main reason for the poor performance of the conventional analysis in this case is the specification of a laterally uniform inflow boundary condition. Without performing a simulation of the entire wind tunnel, the only basis for determining an appropriate inlet profile for a conventional CFD analysis would be the measurements performed in the (empty) wind tunnel. Note that, even with the knowledge of "inlet" profiles at three positions along the test section width, the flow appears to be laterally uniform (Fig. 4a), due to the unfortunate position of the P03-measurements relative to the position of the vertical guiding vane. Hence, a uniform inlet profile would be a logical choice, leading however to erroneous results.

7 Discussion

A number of assumptions have been made in numerically modeling the entire wind tunnel. Most of these were verified by sensitivity analyses, as indicated earlier. The assumption that was not verified by sensitivity analysis was the modeling of the fan-straightener section and heat exchanger, i.e. replacing the fan (with rotating fan blades, fan nacelle, supports), straighteners and heat exchanger by a simple polynomial representing the fan boundary condition without swirl. However, this assumption was validated – as far as the flow conditions in the test section are concerned – by the comparison with the measurements. A good agreement was found, both for the case of the empty wind tunnel and for the case of the wind tunnel with building model. Nevertheless, future research should focus on the effect of these features on the flow. As an example, the head loss over the heat exchanger should be incorporated separately in future studies.

The proposed model is only validated for a limited number of cases and at a limited number of points, all situated in the test section and situated upstream and one at the side of the building model. Future research should include comparisons with measured data in the wake of the building and preferably also in other sections of the wind tunnel. Other turbulence models might be needed to achieve good numerical predictions at these positions. On the other hand, it is important to note that, despite the multiple flow separations that occur both in the real and in the numerical wind tunnel, the numerical methodology in combination with the k-ε model provides accurate results in the test section downstream of these separations.

Modeling the flow conditions in the entire wind tunnel requires more effort than only modeling the flow in the test section. A relatively large number of grid cells were required to model the flow through the slatted screen and around the guiding vanes (Table 5). Relatively few cells were used in the other parts of the tunnel. Due to the use of the special fan boundary condition, the number of required cells in the fan-straightener section was quite low. Nevertheless, compared to the conventional approach, the calculation time increased by a factor 4. It was shown in this paper that this increase in effort and time can provide significantly more accurate numerical results. The choice for one approach or the other will depend on the situation and on the objectives. Deviations of the wind tunnel configuration from the requirements for boundary layer wind tunnels mentioned in section 2 (no lateral uniformity, separation in the circuit, large blockage ratio, a forced small wake) are aspects in favor of the proposed approach.

The proposed numerical methodology can be extended to open-circuit wind tunnels. This will generally imply the need to include the surrounding environment of the wind tunnel in the numerical model.

8 Conclusions

A methodology has been presented to accurately model the flow conditions in the test section of closed-circuit wind tunnels. The methodology is based on numerically modeling the entire wind tunnel, determining the relationship between the total pressure loss and the flow rate and implementing a fan performance curve that intersects the system curve at the operating point at which the measurements have been or will be conducted. The actual shape of the fan performance curve can be chosen arbitrarily. The only requirement is intersecting the system curve in the operating point. The shape of the fan curve however does determine to a large extent the calculation time.

The proposed methodology was applied and validated for the Thermal Circuit of the Jules Verne climatic wind tunnel, for the case of an empty test section and for the case of a block-type building placed in the test section. It was shown that for these cases, the simulation results generally reproduced the measurements within 10% accuracy. This accuracy is 2 to 4 times better than the results obtained by a conventional CFD analysis of the same tunnel which employs a rectangular computational domain instead of a closed-circuit computational domain. For wind tunnels with a more carefully designed return leg the difference in accuracy between the conventional analysis and the proposed methodology will be less pronounced. The poor performance of the conventional analysis for this wind tunnel shows the influence of incomplete data for the boundary conditions on the agreement between experiment and simulation and the necessity of detailed approach flow data for validation purposes. Modeling the entire wind tunnel is one method of obtaining such detailed data.

The methodology developed in this paper and the accuracy obtained provide perspectives for the use of this methodology and of CFD in general as a tool in wind tunnel design and testing and for CFD validation studies when detailed boundary (inlet) conditions are not available.

9 Acknowledgements

This research was funded by the IWT-Flanders (Institute for the Promotion of Innovation by Science and Technology in Flanders). This institute supports and stimulates industrial research and technology transfer in the Flemish industry. The second author is a post-doctoral fellow of the FWO-Flanders (Research Fund) that supports fundamental research in Flanders. The financial support by both institutions is gratefully acknowledged.

The measurement data used in this study were obtained as a result of the participation of the authors in the European Commission Fourth Framework Program (Training and Mobility of Researchers, Access to Large Scale Facilities – Access for researchers). The authors want to express their gratitude to the European Commission and to our partners in the measurement project: Fabien van Mook (Technical University of Eindhoven) and Carl-Eric Hagentoft (Chalmers University of Technology). Special appreciation is also expressed to the CSTB (Centre Scientifique et Technique du Bâtiment, Nantes, France), in particular to Philippe Delpech, Marc Dufresne de Virel and Jean-Paul Flori for their help during the wind tunnel tests.

10 References

[1] T. Stathopoulos, Design and fabrication of a wind tunnel for building aerodynamics. Journal of Wind Engineering and Industrial Aerodynamics, 16 (1984) 361-376.

[2] S.O. Hansen, E.G. Sorensen, A new boundary-layer wind tunnel at the Danish Maritime Institute. Journal of Wind Engineering and Industrial Aerodynamics, 18 (1985) 213-224.

[3] J.E. Cermak, L.S. Cochran, Physical modeling of the atmospheric surface layer, Journal of Wind Engineering and Industrial Aerodynamics 41-44 (1992) 935-946.

[4] H.J. Niemann, The boundary layer wind tunnel: an experimental tool in building aerodynamics and environmental engineering. Journal of Wind Engineering and Industrial Aerodynamics 48 (1993) 145-161.

[5] M. Schatzmann, J. Donat, S. Hendel, G. Krishan, Design of a low-cost stratified boundary-layer wind tunnel, Journal of Wind Engineering and Industrial Aerodynamics 54/55 (1995) 483-491.

[6] J.E. Cermak, Wind-tunnel development and trends in applications to civil engineering. Journal of Wind Engineering and Industrial Aerodynamics 91 (3) (2003) 355-370.

[7] C.H. Chang, R.N. Meroney, The effect of surroundings with different separation distances on surface pressures on low-rise buildings, Journal of Wind Engineering and Industrial Aerodynamics 91 (8) (2003) 1039-1050.

[8] J.D. Ginger, J.D. Holmes, Effect of building length on wind loads on low-rise buildings with a steep roof pitch, Journal of Wind Engineering and Industrial Aerodynamics 91 (11) (2003) 1377-1400.
[9] P. Delpech, P. Palier, J. Gandemer, Snowdrifting simulation around Antarctic buildings, Journal of Wind Engineering and Industrial Aerodynamics 74-6 (1998) 567-576.
[10] A.P.G. Sagrado, J. van Beeck, P. Rambaud, D. Olivari, Numerical and experimental modelling of pollutant dispersion in a street canyon, Journal of Wind Engineering and Industrial Aerodynamics 90 (4-5) (2002) 321-339.
[11] T. Stathopoulos, H.Q. Wu, Wind-tunnel techniques for assessment of pedestrian-level winds, Journal of Engineering Mechanics – ASCE 119 (10) (1993) 1920-1936.
[12] D. Surry, D.R. Inculet, P.F. Skerlj, J.X. Lin, A.G. Davenport, Wind, rain and the building envelope – a status report of ongoing research at the University of Western Ontario, Journal of Wind Engineering and Industrial Aerodynamics 53 (1994) 19-36.
[13] B. Blocken, J. Carmeliet, A review of wind-driven rain research in building science, Journal of Wind Engineering and Industrial Aerodynamics 92 (13) (2004) 1079-1130.
[14] R.N. Meroney, B.M. Leitl, S. Rafailidis, M. Schatzmann, Wind-tunnel and numerical modeling of flow and dispersion about several building shapes, Journal of Wind Engineering and Industrial Aerodynamics 81 (1999) 333-345.
[15] T. Stathopoulos, The numerical wind tunnel for industrial aerodynamics: Real or virtual in the new millennium? Wind and Structures 5 (2-4) (2002) 193-208.
[16] B.M. Leitl, R.N. Meroney, Car exhaust dispersion in a street canyon. Numerical critique of a wind tunnel experiment, Journal of Wind Engineering and Industrial Aerodynamics 67-8 (1997) 293-304.
[17] R. Gordon, M.S. Imbabi, CFD simulation and experimental validation of a new closed circuit wind/water tunnel design, Journal of Fluids Engineering – Transactions of the ASME 120 (2) (1998) 311-318.
[18] S.A.A.A. Ghani, A. Aroussi, E. Rice, Simulation of road vehicle natural environment in a climatic wind tunnel , Simulation Practice and Theory 8 (6-7) (2001) 359-375.
[19] J.J. Korte, Aerodynamic design of axisymmetrical hypersonic wind-tunnel nozzles using a least-squares parabolized Navier-Stokes procedure. Journal of Spacecraft and Rockets 29 (5) (1992) 685-691.
[20] S. Moreau, M. Henner, M. Roger, Analysis of flow conditions in freejet experiments for studying airfoil self-noise, AIAA Journal 41 (10) (2003) 1895-1905.
[21] C.E. Cockrell, Interpretation of waverider performance data using Computational Fluid Dynamics, Journal of Aircraft, 31(5) (1994): 1095-1100.
[22] S.S. Desai, Relative roles of computational fluid dynamics and wind tunnel testing in the development-of aircraft, Current Science 84(1) (2003) 49-64.
[23] J. Franke, C. Hirsch, A.G. Jensen, H.W. Krüs, M. Schatzmann, P.S. Westbury, S.D. Miles, J.A. Wisse, N.G. Wright, Recommendations on the use of CFD in predicting pedestrian wind environment. Journal of Wind Engineering and Industrial Aerodynamics, Submitted.
[24] A. Baskaran, T. Stathopoulos, Influence of computational parameters on the evaluation of wind effects on the building envelope. Building and Environment 27(1) (1992) 39-49.
[25] B. Blocken, S. Roels, J. Carmeliet, Modification of pedestrian wind comfort in the Silvertop Tower passages by an automatic control system, Journal of Wind Engineering and Industrial Aerodynamics 92(10) (2004) 849-873.
[26] J.B. Barlow, W.H. Rae, A. Pope, Low-speed wind tunnel testing. Third Edition, John Wiley & Sons. 1999.
[27] F. Baetke, H. Werner, Numerical simulation of turbulent flow over surface-mounted obstacles with sharp edges and corners, Journal of Wind Engineering and Industrial Aerodynamics, 35 (1990) 129-147.
[28] J. Gandemer, La soufflerie climatique “Jules Verne”, Journal of Wind Engineering and Industrial Aerodynamics, 41-44 (1992) 43-54.
[29] W.P. Jones, B.E. Launder, The prediction of laminarization with a 2-equation model of turbulence. International Journal of Heat and Mass Transfer 15 (1972) 301.
[30] T.-H. Shih, W.W. Liou, A. Shabbir, Z. Yang, J. Zhu, A new k-ε eddy viscosity model for high Reynolds number turbulent flows, Computers & Fluids, 24 (1995) 227-238.
[31] B.E. Launder, D.B. Spalding, The numerical computation of turbulent flows, Computer Methods in Applied Mechanics and Engineering, 3 (1974) 269-289.
[32] S.-E. Kim, D. Choudhury, A near-wall treatment using wall functions sensitized to pressure gradient, ASME FED, 217 (1995) 273-280.

[33] P. Vandoormaal, G. D. Raithby, Enhancements of the SIMPLE Method for Predicting Incompressible Fluid Flows, Numerical Heat Transfer, 7 (1984) 147-163.
[34] Leonard, B.P. A Stable and Accurate Convection Modelling Procedure Based on Quadratic Upstream Interpolation. Computer Methods in Applied Mechanics and Engineering, 19 (1979) 59-98.
[35] Fluent Inc., Fluent 5 User's Guide, Lebanon, New Hampshire, 1998.

Symbol list

a_0	First polynomial coefficient of fan performance curve	Pa
a_1	Second polynomial coefficient of fan performance curve	Pa.s/m
A_{fan}	Cross-sectional area of the wind tunnel at the fan position	m²
C_{KS}	Roughness constant	-
G_a	Volumetric flow rate	m³/s
I_U, I_V, I_W	Turbulence intensity in streamwise, vertical and lateral direction	%
k	Turbulent kinetic energy	m²/s²
K_S	Physical roughness height	m
ℓ	Number indicating wind tunnel section	-
L	Length	m
L_ℓ	Length of wind tunnel section ℓ	m
P	Pressure	Pa
ΔP_{tot}	Total pressure loss	Pa
R_ℓ	Frictional losses per unit length	Pa/m
u, v, w	Instantaneous velocity components in streamwise, vertical and lateral direction	m/s
U, V, W	Average velocity components in streamwise, vertical and lateral direction	m/s
w, d, h	width, depth and height of the building model	m
W, H	width and height of a cross-section in the wind tunnel	m
X, Y, Z	Streamwise, vertical and lateral cartesian co-ordinates	m
y^+	Dimensionless wall unit	-
ε	Turbulence dissipation rate	m²/s³
Φ	Diameter	m
ρ	Air density	kg/m³
ξ	Loss coefficient	$(Pa.s^2)/m^6$

FIGURE CAPTIONS

Fig. 1: (a) Plan view, (b) longitudinal cross-sectional view, (d) lateral cross-sectional view and (c) photograph of nozzle, screen and guiding vanes of the thermal circuit of the Jules Verne wind tunnel facility. The different sections and features of the wind tunnel are indicated with numbers. All dimensions are given in meter.

Fig. 2: Top view of the test section with indication of the measurement positions for (a) the case of an empty test section and (b) with the building model in the test section.

Fig. 3: (a) Mean streamwise wind speed profiles (U) and (b) longitudinal turbulence intensity profiles (I_U) at position P01 for the 3 free-run experiments (wind tunnel speed settings 1.6 m/s, 3.6 m/s and 5.5 m/s).

Fig. 4: (a) Mean streamwise wind speed profiles (U) and (b) longitudinal turbulence intensity profiles (I_U) at the positions P01-P04 for a free-run experiment (wind tunnel speed setting 5.5 m/s).

Fig. 5: (a) Model of the geometry of the entire closed-circuit wind tunnel with a fan boundary condition. (b) Model of only the test section of the wind tunnel with an inlet and an outlet boundary condition (conventional approach).

Fig. 6: Graphical representation of the system curve, three different fan performance curves and the corresponding operating points.

Fig. 7: Graphical representation of the system curve and three different fan performance curves, all yielding the same operating point and the same solution, but different convergence rates.

Fig. 8: View of the computational mesh at the surfaces of (a) the guiding vanes, screen and nozzle exit and (b) the building model and floor in the test section.

Fig. 9: Contours of the wind speed (magnitude of the 3D velocity vector) in the empty wind tunnel (a) in a horizontal plane at a height of 1.75 m above the test section floor and (b) in a vertical plane along the test section center line. The measurement positions are indicated.

Fig. 10: Comparison between the dimensionless wind speed measurements and the corresponding calculations for all 48 measurement points in the empty wind tunnel. All data are made dimensionless with respect to the streamwise velocity at 2.1m height on the vertical line P01 and averaged over the 3 velocity regimes. ±The 10% error lines are indicated.

Fig. 11: Comparison between the measured turbulence intensity profiles, averaged over the three velocity regimes and the corresponding calculations (a) at P03 and (b) at P04.

Fig. 12: Contours of the wind speed (magnitude of the 3D velocity vector) in the wind tunnel with building model (a) in a horizontal plane at a height of 1.75 m above the test section floor and (b) in a vertical plane along the test section center line. The measurement positions are indicated.

Fig. 13: Comparison between the dimensionless measured velocity components and the corresponding calculations for all 6 measurement positions around the building model. All data are made dimensionless with respect to the streamwise velocity at 2.1m height on the vertical line P01 and averaged over the 3 velocity regimes. The 10% error lines are indicated.

Fig. 14: Comparison between the measured turbulence intensity and the corresponding calculations for all 6 measurement positions around the building model. The data are averaged over the 3 velocity regimes. The dotted lines indicate deviations from the measurement value, relative to this value.

Fig. 15: Comparison between the dimensionless measured x-velocity components for all 6 measurement positions around the building model and the corresponding calculations in a rectangular (r) and a closed-circuit (c) domain. The dotted lines indicate deviations from the measurement value, relative to this value.

Figure 1-color (web version)

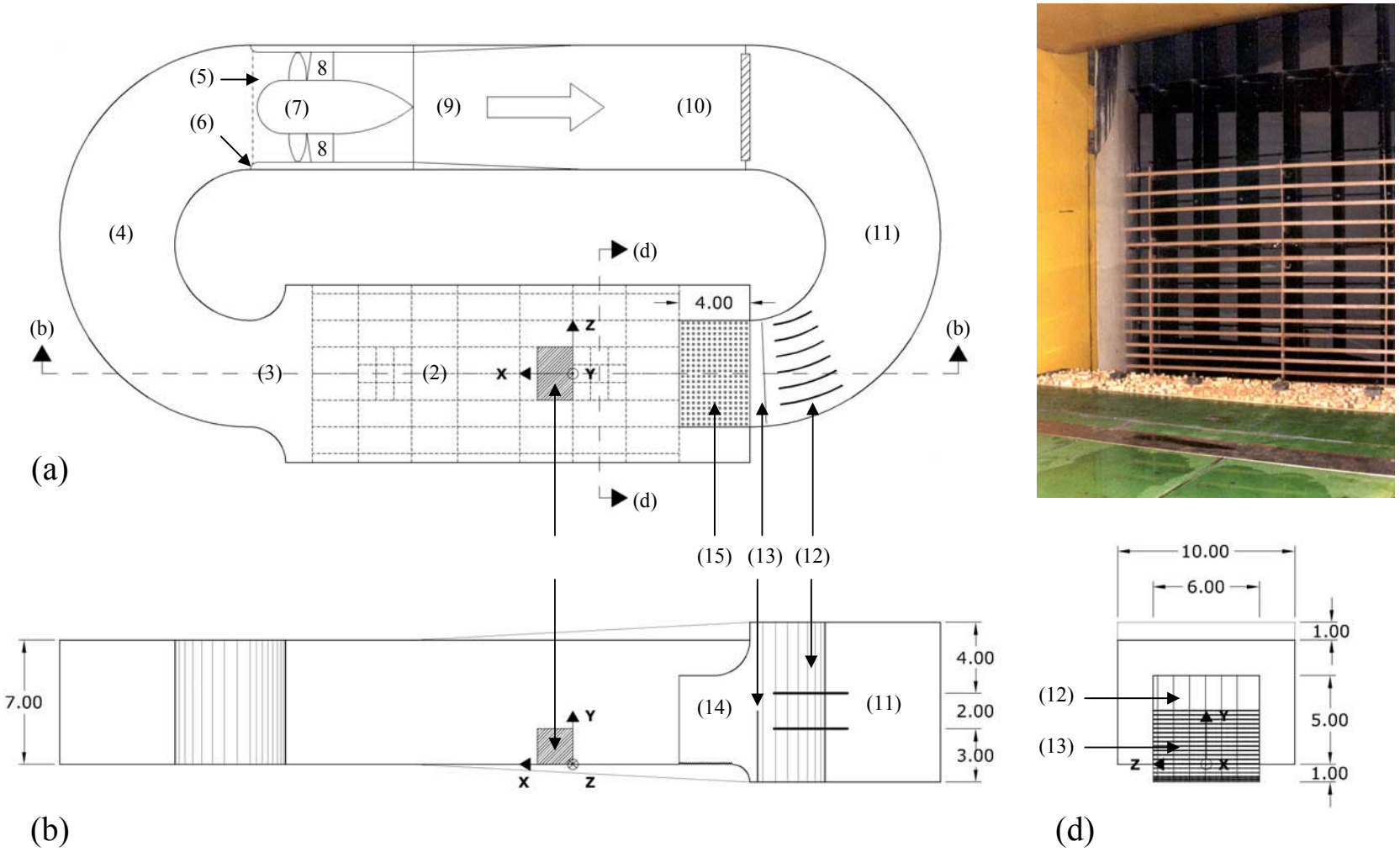

Figure 1-grayscale (printed version)

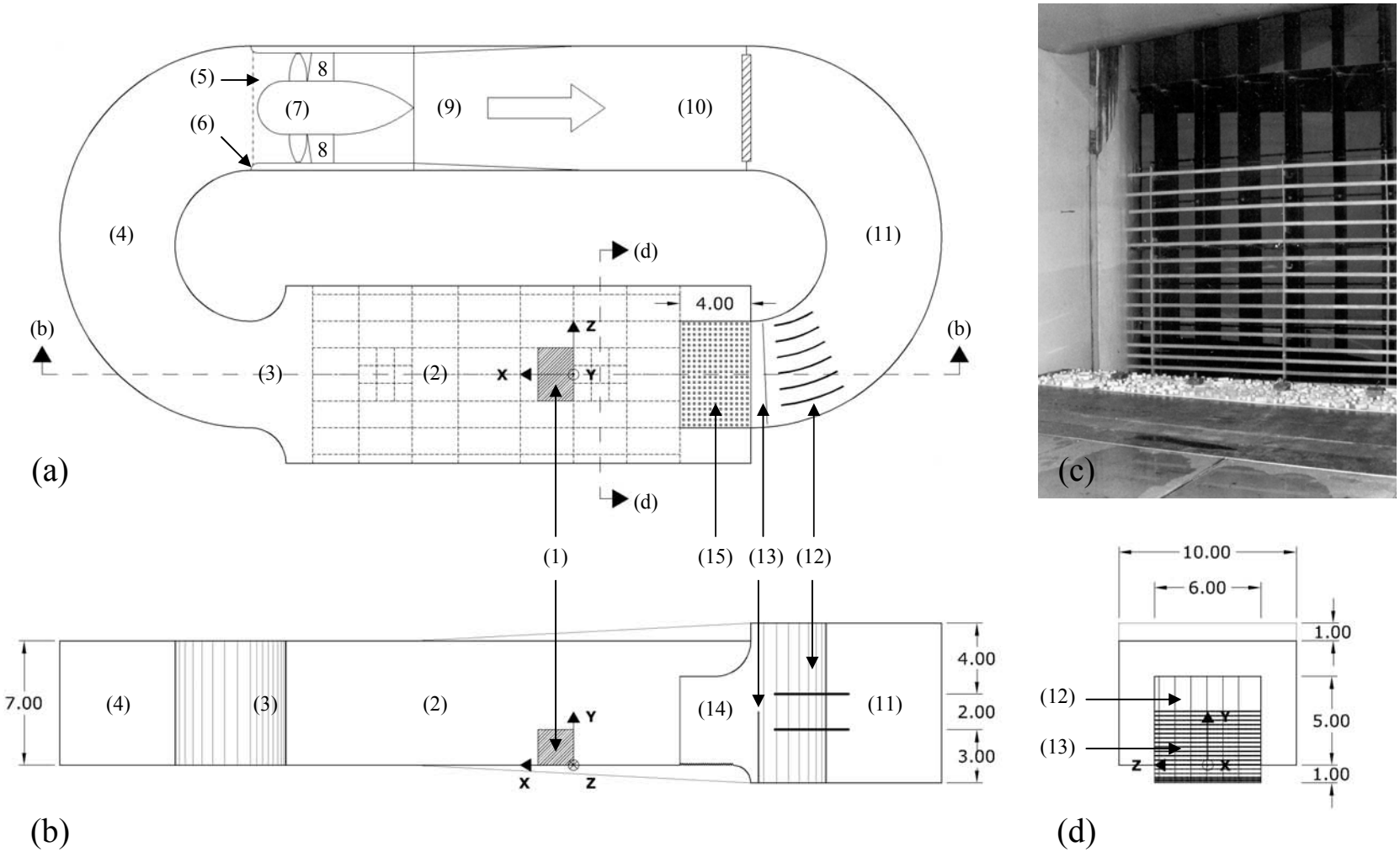

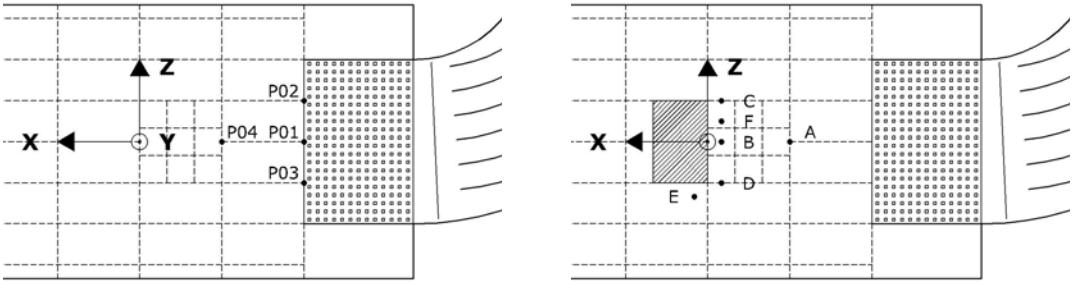

(a) (b)

FIG. 2

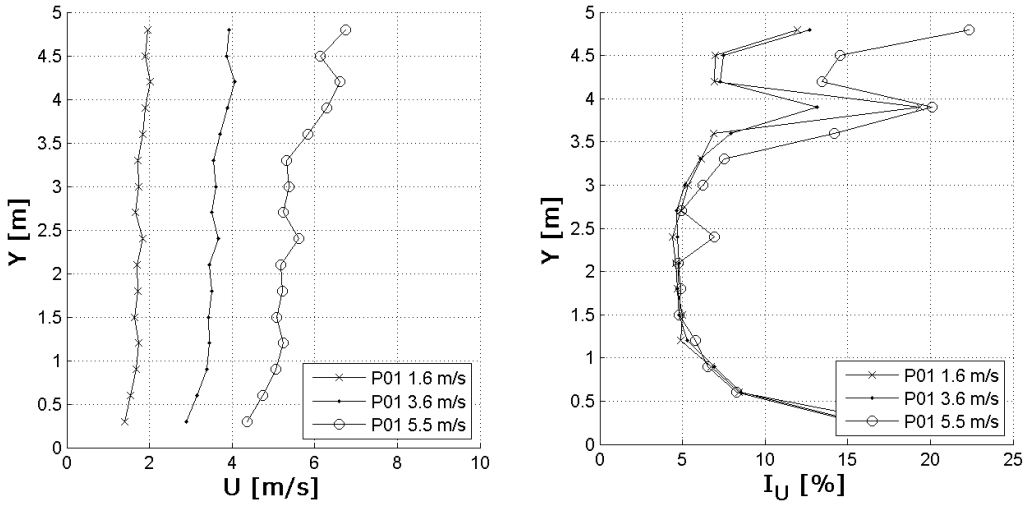
Y [m]
U [m/s]
P01 1.6 m/s
P01 3.6 m/s
P01 5.5 m/s
Y [m]
I_U [%]
P01 1.6 m/s
P01 3.6 m/s
P01 5.5 m/s

(a) (b)

FIG. 3

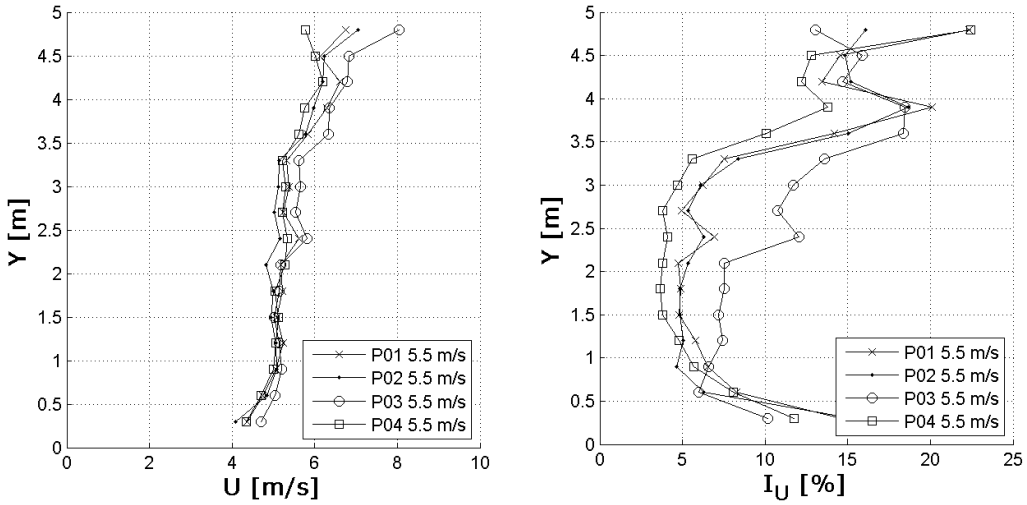
Y [m]
U [m/s]
P01 5.5 m/s
P02 5.5 m/s
P03 5.5 m/s
P04 5.5 m/s
Y [m]
I_U [%]
P01 5.5 m/s
P02 5.5 m/s
P03 5.5 m/s
P04 5.5 m/s

(a) (b)

FIG. 4

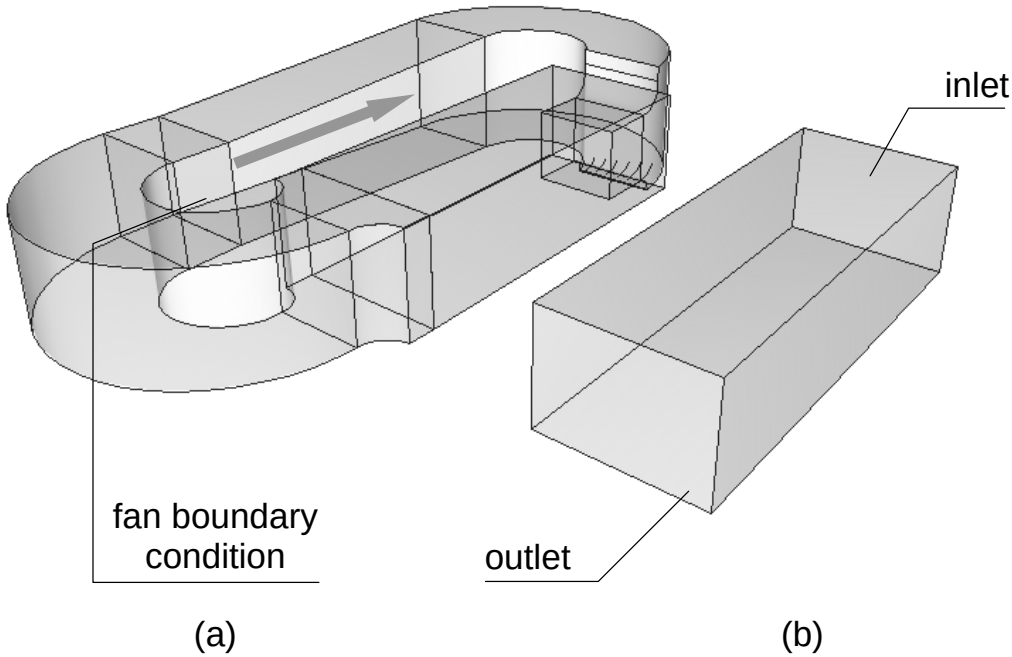

FIG. 5

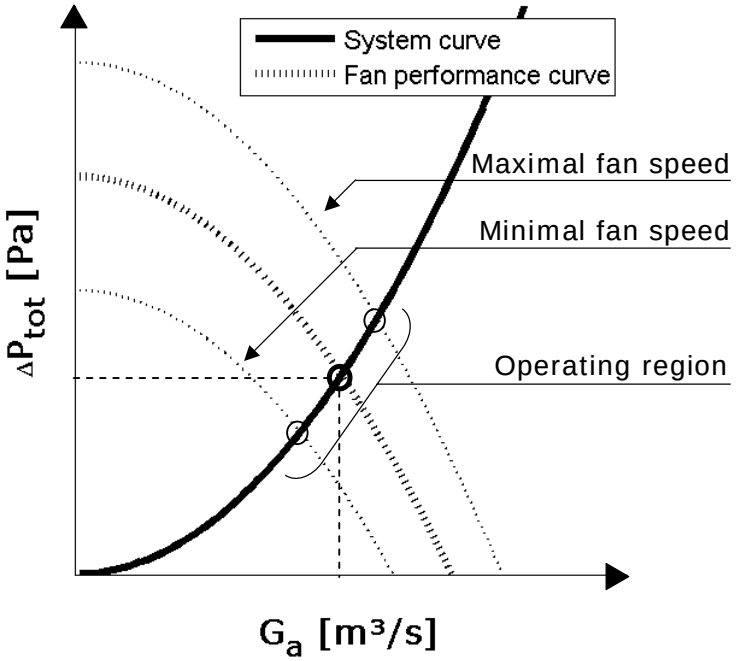
System curve
Fan performance curve
Maximal fan speed
Minimal fan speed
Operating region
ΔP_tot [Pa]
G_a [m³/s]

FIG. 6

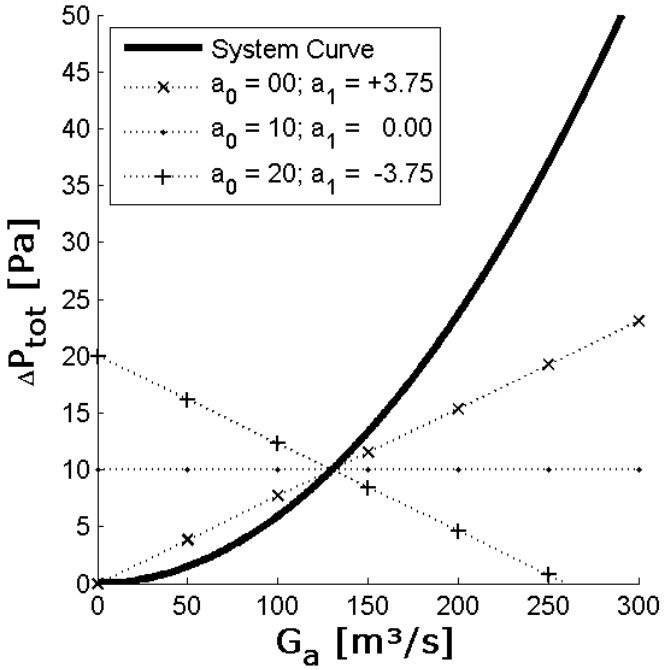
System Curve
a0 = 00; a1 = +3.75
a0 = 10; a1 = 0.00
a0 = 20; a1 = -3.75
ΔPtot [Pa]
Ga [m³/s]
0
5
10
15
20
25
30
35
40
45
50
0
50
100
150
200
250
300

FIG. 7

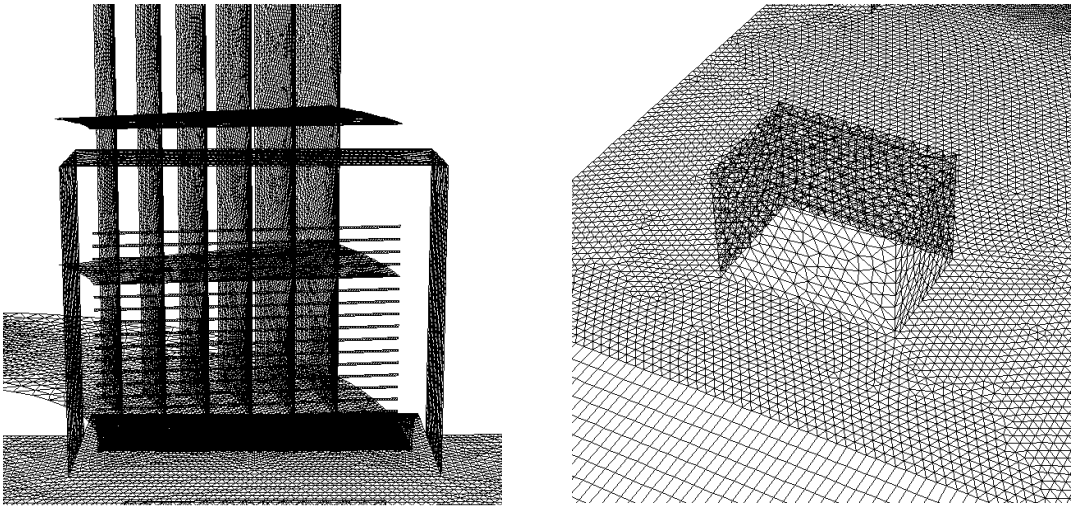

(a) (b)

FIG. 8

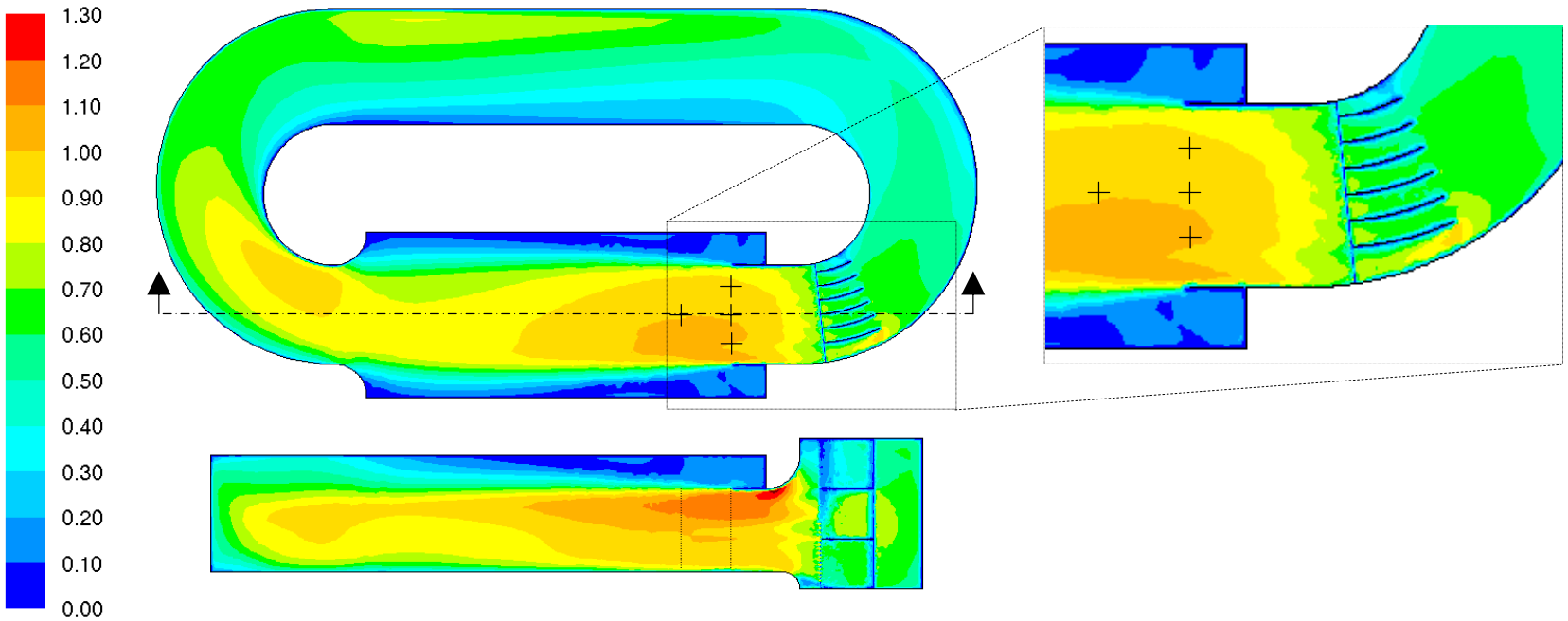

FIG. 9-color (web version)

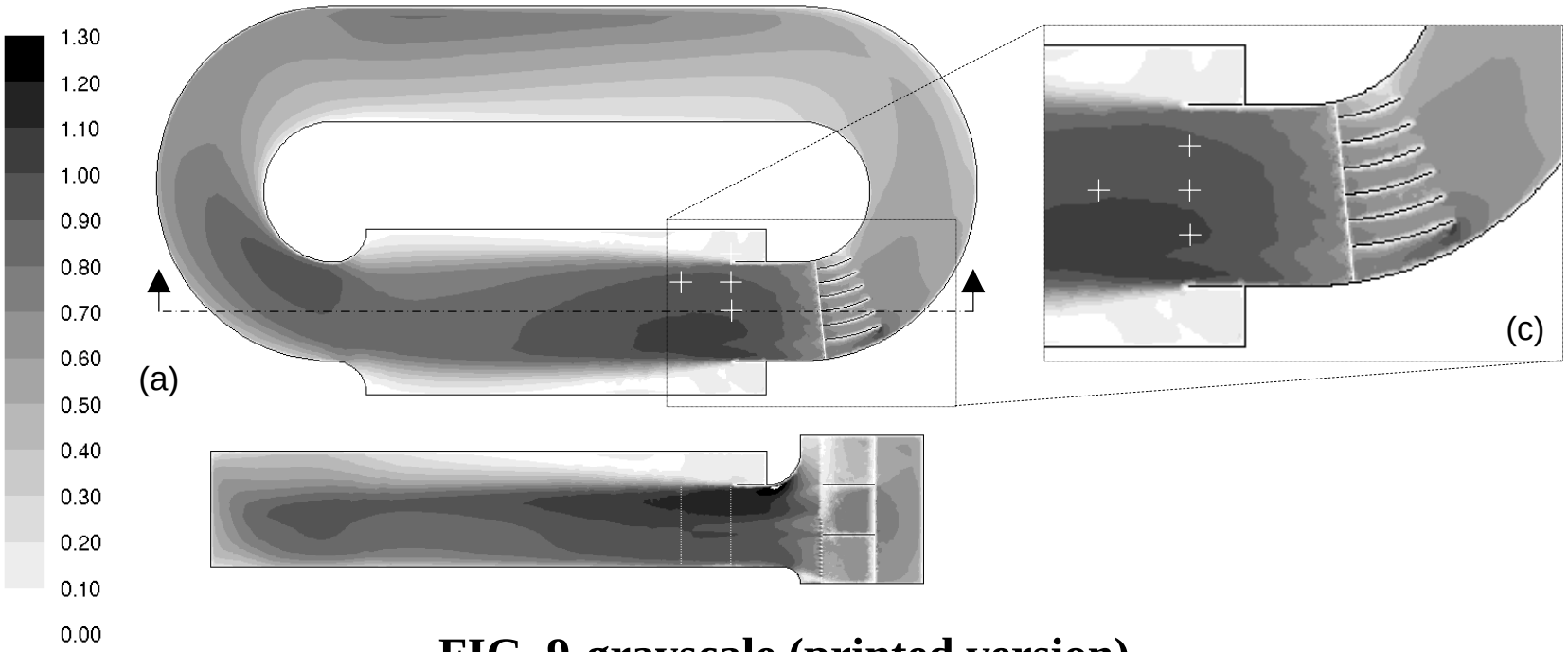

FIG. 9-grayscale (printed version)

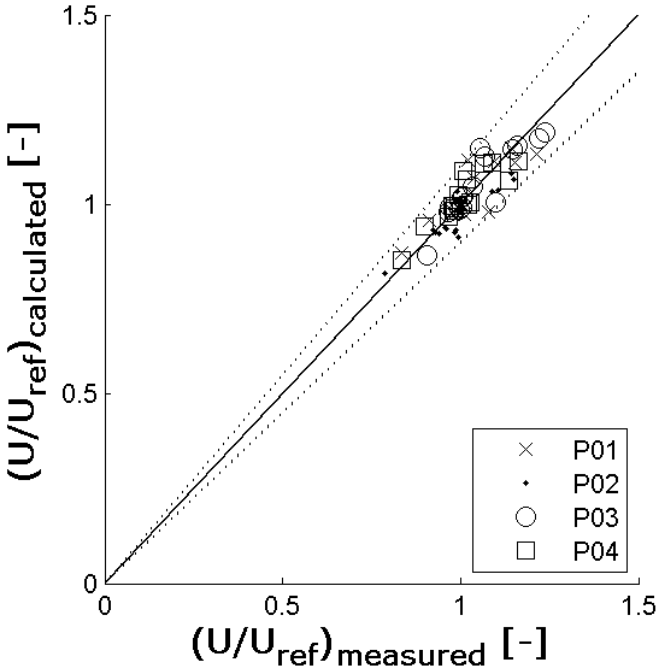
1.5
1
0.5
0
0
0.5
1
1.5
$(U/U_{ref})_{calculated}$ [-]
$(U/U_{ref})_{measured}$ [-]
P01
P02
P03
P04

FIG. 10

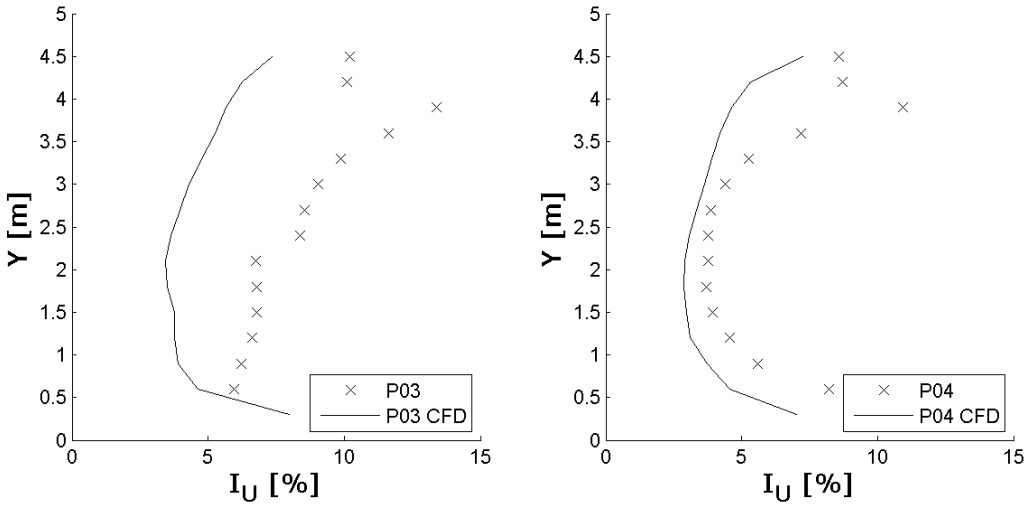

(a) (b)

FIG. 11

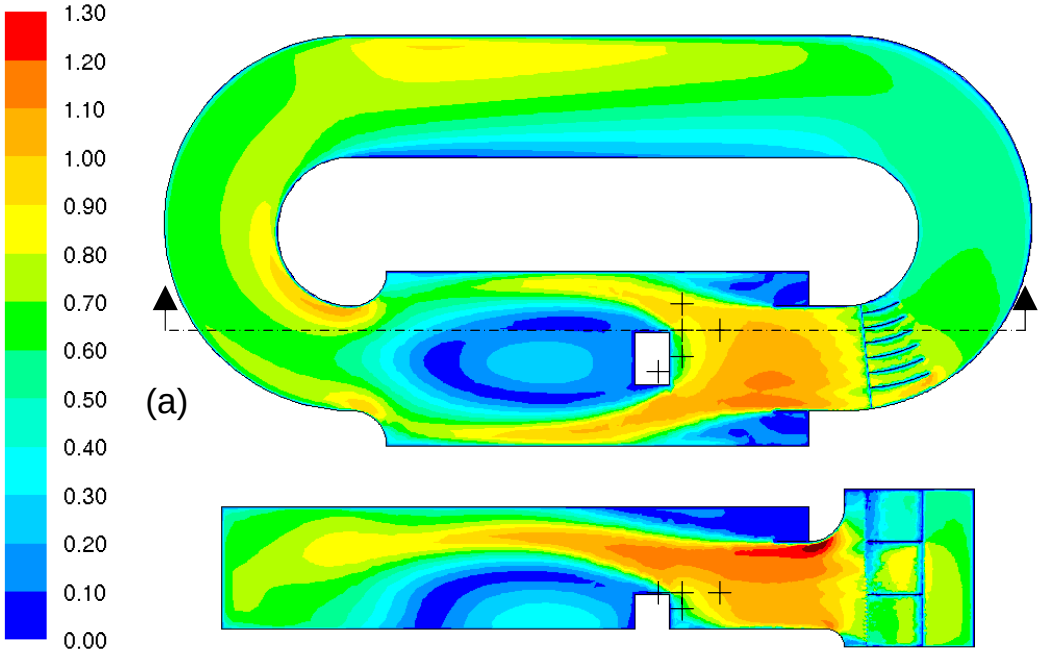

FIG. 12-color (web version)

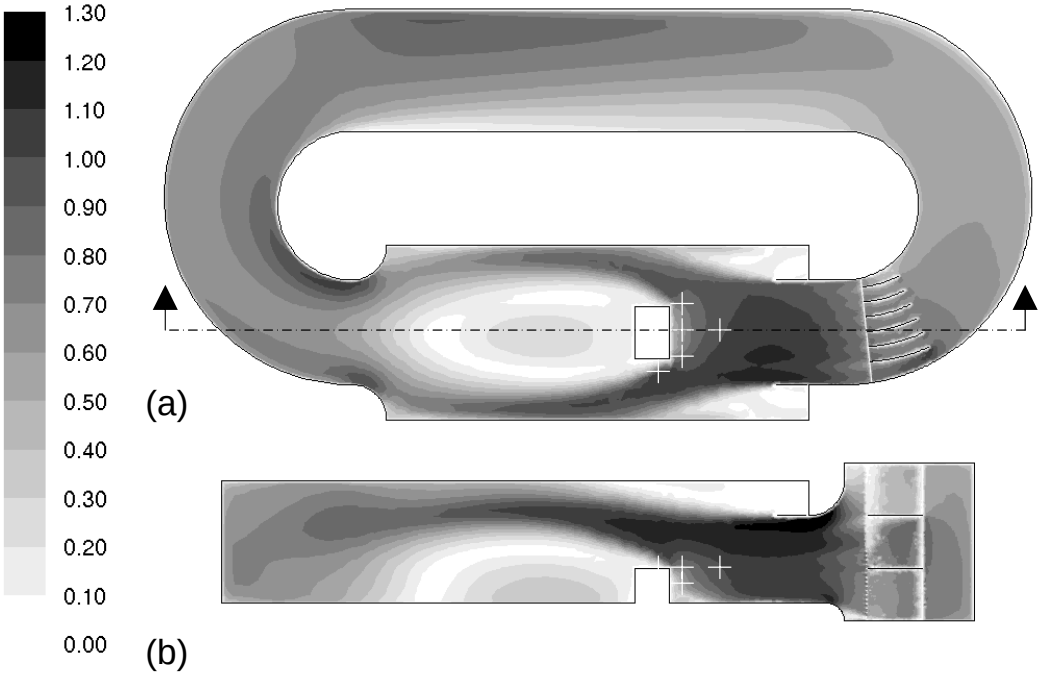

FIG. 12-grayscale (printed version)

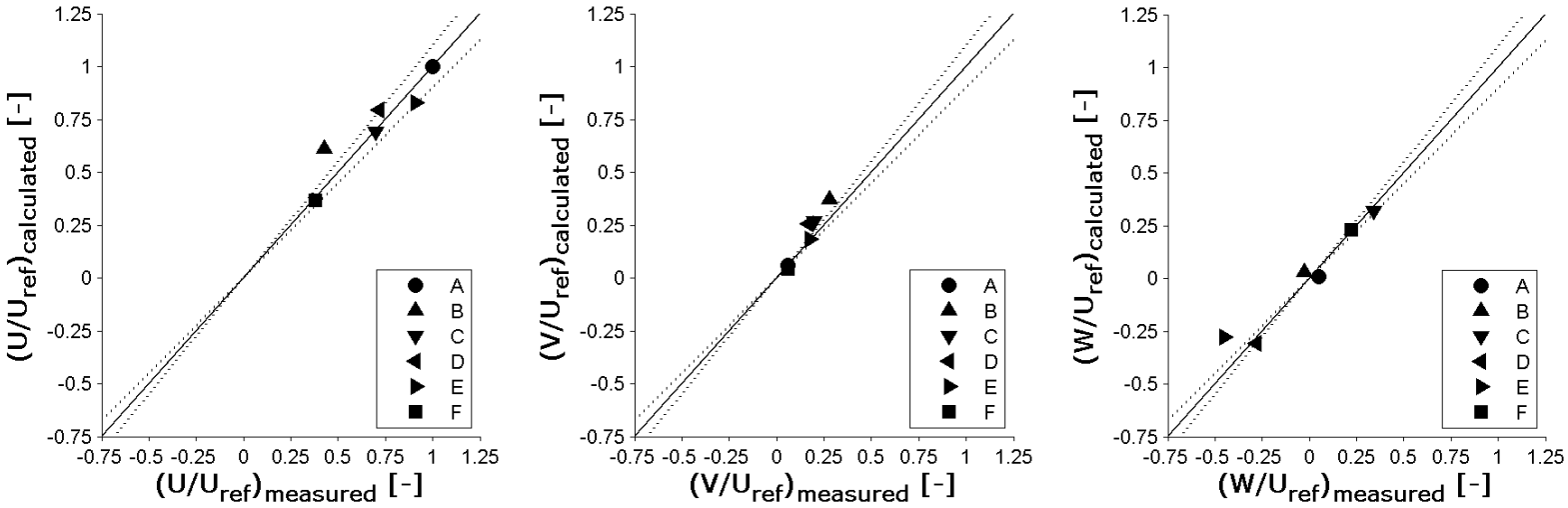
1.25
1
0.75
0.5
0.25
0
-0.25
-0.5
-0.75
-0.75 -0.5 -0.25 0 0.25 0.5 0.75 1 1.25
(U/U_ref)_calculated [-]
(U/U_ref)_measured [-]
(V/U_ref)_calculated [-]
(V/U_ref)_measured [-]
(W/U_ref)_calculated [-]
(W/U_ref)_measured [-]
A
B
C
D
E
F

FIG. 13

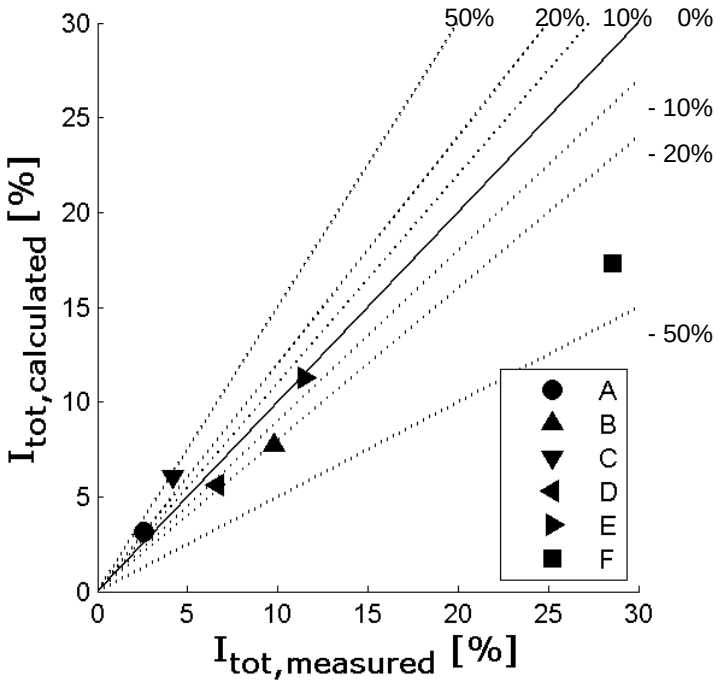
50%
20%
10%
0%
- 10%
- 20%
- 50%
A
B
C
D
E
F
$I_{tot,calculated}$ [%]
$I_{tot,measured}$ [%]
0
5
10
15
20
25
30

FIG. 14

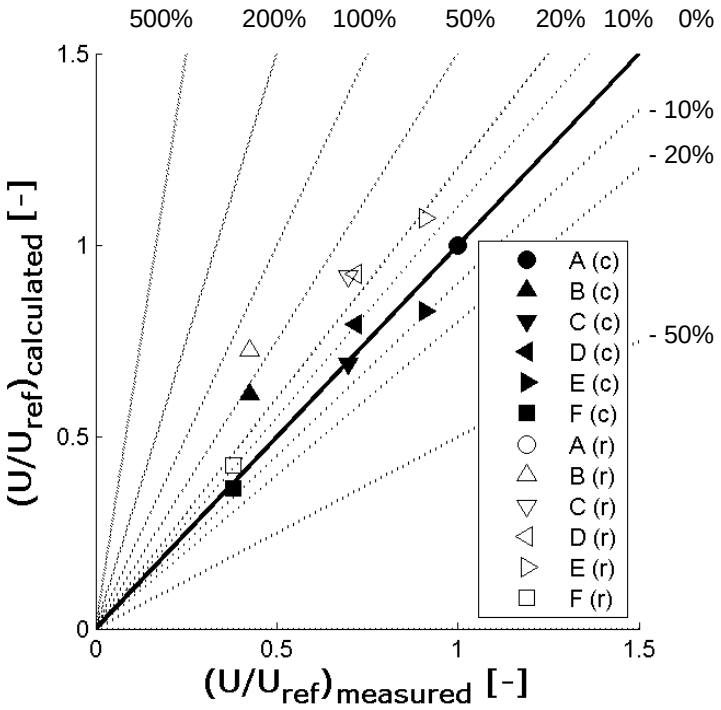
500%
200%
100%
50%
20%
10%
0%
- 10%
- 20%
- 50%
1.5
1
0.5
0
0
0.5
1
1.5
(U/U_ref)_calculated [-]
(U/U_ref)_measured [-]
A (c)
B (c)
C (c)
D (c)
E (c)
F (c)
A (r)
B (r)
C (r)
D (r)
E (r)
F (r)

FIG. 15

Table 1: Co-ordinates of the measurement points, relative to the windward facade of the building model (whether present or not). The co-ordinate system is indicated in Fig. 2.

Profile/Point	X [m]	Y [m]	Z [m]
P01	-6.00	0.30 - 4.80	0.00
P02	-6.00	0.30 - 4.80	1.50
P03	-6.00	0.30 - 4.80	-1.50
P04	-3.00	0.30 - 4.80	0.00
A	-3.00	2.05	0.00
B	-0.50	2.05	0.00
C	-0.50	2.05	1.50
D	-0.50	2.05	-1.50
E	0.50	2.05	-2.00
F	0.50	1.18	0.75

Table 2: Measured components of mean velocity (U, V, W) (streamwise, vertical and lateral) and turbulence intensity (I_U, I_V, I_W) at points A-F around the building model. The wind speed values are made dimensionless by division by the streamwise wind speed (U) in point A and averaged over the three flow regimes. The turbulence intensities are also averaged over the flow regimes. The figures in the left column indicate the flow direction and the position of the measurement points relative to the building model.

Position	Z / X / Y	U [-]	V [-]	W [-]	I_U [%]	I_V [%]	I_W [%]
A	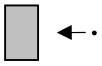	1.00	0.06	-0.05	1.66	1.51	1.30
B	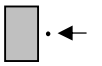	0.42	0.28	-0.03	8.44	3.59	3.44
C	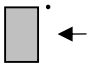	0.70	0.20	0.34	2.72	2.53	1.90
D	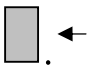	0.72	0.17	-0.28	5.54	2.43	2.68
E	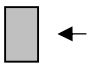	0.91	0.17	-0.45	8.74	5.16	5.30
F	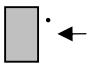	0.38	0.06	0.22	22.98	11.84	12.19

Table 3: Applied physical roughness heights K_S and roughness constants C_{KS} for different parts of the wind tunnel.

Boundary surface	K_S	C_{KS}
Floor	10^{-3} m	0.5
Floor with densily spaced roughness elements	5×10^{-2} m	0.5
Wall	10^{-3} m	0.5
Ceiling	10^{-3} m	0.5
Guiding vanes	10^{-6} m	0.5
Screen slats	10^{-3} m	0.5

Table 4: Grid sensitivity analysis: number of control volumes (cells) for each grid. The grids that were selected from this analysis are underlined.

Case	Grid Name	Number of cells
Empty wind tunnel	G1	2 066 637
	G2	888 133
	G3	670 965
	G4	394 433
Wind tunnel with building model	G3a	669 836
	G3b	693 833
	G3c	737 299

Table 5: Distribution of control volumes in the (empty) wind tunnel.

Wind tunnel section	Grid type	Number of CVS
Test section (2)	Mixed	371 586[1]
Section transition (3)	Tetrahedral	24 178
First 180° turn (4)	Prismatic	30 828
Fan section (7,8)	Prismatic	2 936
Diffuser + heat exchanger (9,10)	Prismatic	46 242
Second 180° turn (11)	Prismatic	34 385
Guiding vanes + Screen (12,13)	Tetrahedral	74 967
Screen + Nozzle (13,14,15)	Tetrahedral	85 843

[1]Approximately half of the number of control volumes in the test section are situated in the transition region from the test section mesh to the (finer) mesh in the nozzle section.